PHYSICAL REVIEW B **105**, 125407 (2022)

Pseudogauge field driven acoustoelectric current in two-dimensional hexagonal Dirac materials

Pankaj Bhalla,[1] Giovanni Vignale,[2] and Habib Rostami[1]

[1]Nordita, KTH Royal Institute of Technology and Stockholm University, Hannes Alfvéns väg 12, 10691 Stockholm, Sweden
[2]Department of Physics and Astronomy, University of Missouri, Columbia, Missouri 65211, USA

(Received 23 December 2021; accepted 1 March 2022; published 10 March 2022)

Using a diagrammatic scheme, we study the acoustoelectric effects in two-dimensional (2D) hexagonal Dirac materials due to the sound-induced pseudogauge field. We analyze both uniform and *spatially dispersive* currents in response to copropagating and counterpropagating sound waves, respectively. In addition to the longitudinal acoustoelectric current, we obtain an exotic *transverse* charge current flowing perpendicular to the sound propagation direction owing to the interplay of transverse and longitudinal gauge field components $j_T \propto A_L A_T^*$. In contrast to the almost isotropic directional profile of the longitudinal uniform current, a highly anisotropic transverse component $j_T \sim \sin(6\theta)$ is achieved that stems from the inherited threefold symmetry of the hexagonal lattice. However, both longitudinal and transverse parts of the dispersive current are predicted to be strongly anisotropic $\sim \sin^2(3\theta)$ or $\cos^2(3\theta)$. We quantitatively estimate the pseudogauge field contribution to the acoustoelectric current that can be probed in future experiments in graphene and other 2D hexagonal Dirac materials.

DOI: 10.1103/PhysRevB.105.125407

I. INTRODUCTION

The passage of a sound wave through an electronic system creates an oscillating electric field which accelerates the charge carriers and generates an electric current. The acoustoelectric effect (AE) is the dc current that arises to second order in the sound-induced electric field. This intriguing nonlinear phenomenon was first predicted by Parmenter [1] and later discussed by Weinreich [2]. The effect has been observed in different classes of materials such as semiconductors, quantum wires, two-dimensional (2D) electron gas, and heterostructures [3–11]. More recently, it has been recognized that the coupling between the surface acoustic wave (SAW) and electrons in 2D Dirac materials provides an exciting opportunity to investigate charge transport driven by the strain fields associated with the propagating SAW [12–19]. In particular, the AE effect of single-layer graphene has been investigated experimentally, and the AE current has been shown to be tunable by the application of a gate voltage [18].

Traditionally, the magnitude of the sound-induced uniform direct current is obtained from the Weinreich's relation [3,20–22]

$$j^{\rm AE} = -\frac{\mu \Gamma_s I_s}{v_s}, \tag{1}$$

where Γ_s is the sound attenuation, I_s is the sound intensity, v_s is the sound velocity, and μ is the mobility of the carriers. The mobility has opposite sign in electron and hole doped systems. The sound attenuation in conventional (piezoelectric) semiconductors is estimated as $\Gamma_s = K_p^2 \Omega(\sigma/\sigma_m)/[1+(\sigma/\sigma_m)^2]$, where K_p^2 is related to the piezoelectric constant, Ω is the sound frequency, and σ is the longitudinal conductivity of the system, with σ_m being a characteristic conductivity constant [23].

A longitudinal sound wave, with a displacement amplitude u_L and wave vector Q, can induce a scalar potential $V = (\Lambda_P - i\Lambda_D Q)u_L$ [24], where Λ_D and Λ_P stand for two distinct contributions, namely, the deformation and piezoelectric couplings, respectively. Notice that the deformation potential contribution is relatively less relevant in the long-wavelength limit. The SAW on the piezoelectric substrate generates a direct AE current in graphene [25] and is predicted to induce valley acoustoelectric current in transition metal dichalcogenides (TMDs) [26]. However, in Dirac materials there is a third contribution to the AE current that can be formally modeled as the acoustic analog of the photogalvanic effect in response to the sound-induced vector potential $\boldsymbol{A}$ [27–35] (pseudogauge phonons). We refer to this additional contribution as the *acoustogalvanic effect* [36]. Similarly, in 3D Dirac materials a sound-induced orbital magnetization is predicted to arise in the second-order response to a sound-induced vector potential [37].

Despite many studies on the piezoelectric mechanism of the AE effect in a 2D electron gas and in graphene [12–19] the analysis of the acoustoelectric effect in 2D hexagonal Dirac materials is not yet complete. In particular, the relevance of the gauge phonon for the AE effect in graphene has not been discussed to the best of our knowledge. Our aim in this paper is to fill this gap by utilizing the diagrammatic second-order response method. We discuss the AE effect originating from both scalar and vector potentials. The scalar potential is dynamically screened, while the pseudogauge potential is not

---

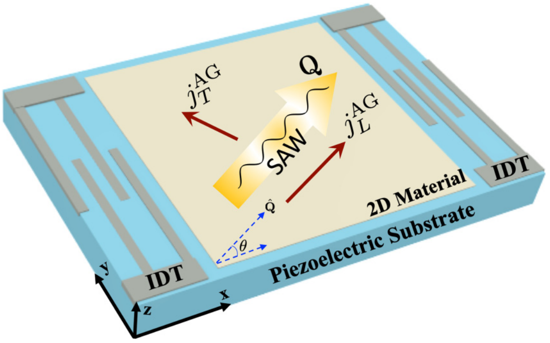

FIG. 1. Schematic experimental setup demonstrating the generation of the acoustogalvanic (AG) currents due to the second-order response to the pseudogauge potential induced by the surface acoustic wave (SAW) propagating in the 2D hexagonal Dirac material placed on a piezoelectric substrate. Interdigital transducers (IDTs) convert electric signals into the SAW with frequency Ω propagating along $\boldsymbol{Q}$ with an elliptic polarization of the displacement fields, $\boldsymbol{u} = u_L\hat{\boldsymbol{Q}} - iu_z\hat{\boldsymbol{z}}$. Here, j_T^{AG} and j_L^{AG} refer to the longitudinal and transverse AG currents, respectively, and θ is an angle obtained by the phonon wave vector with the x direction (zigzag orientation on the hexagonal lattice).

screened because it does not generate a charge current in the linear response.

The conventional AE current, i.e., the current generated by the piezoelectric and deformation potentials, flows parallel to the direction of propagation of the SAW, i.e., it is purely longitudinal: $j_L^{\mathrm{AE}}||\boldsymbol{Q}$. However, the acoustogalvanic (AG) current contains both longitudinal (j_L^{AG}) and transverse (j_T^{AG}) components which are parallel and perpendicular to the sound wave vector, respectively; see the schematic view in Fig. 1. We obtain a nontrivial dependence of the AG current on the sound propagation direction that stems from the implicit threefold symmetry of the 2D hexagonal Dirac material crystal. We quantitatively analyze the frequency, Fermi energy, and angular dependence of the AG current components. Furthermore, in addition to the spatially uniform AG current $j_{L,T}^{\mathrm{AG}}$, we study the spatially dispersive current [38,39] $j_{L,T}^{\mathrm{s-AG}}$, which exhibits a distinctive dependence on the frequency, the Fermi energy, and the propagation angle. The calculated AG current is in good agreement with experimental measurements in graphene [18]. Our calculations are done with the Green's function method, which facilitates the further investigation of the impact of many-body interactions on the AE effect by systematic many-body perturbation theory and *ab initio* approaches.

II. METHOD

A Rayleigh SAW [40] propagating in the xy plane is an elliptically polarized wave in the xz plane:

$$\boldsymbol{u}(\boldsymbol{r},t) = \tfrac{1}{2}(u_L\hat{\boldsymbol{Q}} - iu_z\hat{\boldsymbol{z}})e^{i(\boldsymbol{Q}\cdot\boldsymbol{r}-\Omega t)} + \text{c.c.}, \tag{2}$$

which is propagating on the surface of a piezoelectric substrate along with the phonon wave vector $\boldsymbol{Q} = Q(\cos\theta, \sin\theta)$, with θ being an azimuthal angle. Here, $\theta = 0$ corresponds to the $\hat{x}$ direction with a zigzag orientation on the hexagonal lattice in our convention, and the SAW dispersion follows the relation $\Omega = v_s Q$. Note that u_L and u_z stand for the longitudinal and normal displacement amplitudes, respectively. Here, we systematically study the direct charge current induced by the sound wave.

We consider the total Hamiltonian of the system which encapsulates three main mechanisms that contribute to the AE current originating from different sources of the Dirac electron's coupling to acoustic phonons

$$\mathcal{H} = v_F\hat{\boldsymbol{\sigma}}\cdot(\boldsymbol{p} + e\boldsymbol{A}^{(\tau)}(\boldsymbol{r},t)) + V(\boldsymbol{r},t). \tag{3}$$

Here, v_F is the Fermi velocity, p is the momentum of an electron, σ_i refers to the Pauli matrices, and $V = \Lambda_D(u_{xx} + u_{yy}) + \Lambda_P u_L$ is a scalar deformation potential that describes the coupling of acoustic phonons to electrons in 2D hexagonal Dirac materials, such as graphene, where $u_{ij} = (\partial_i u_j + \partial_j u_i + \partial_i h\partial_j h)/2$ stands for the strain tensor components in terms of the displacement vector $\boldsymbol{u} = (u_x, u_y, h)$ having $h \equiv u_z$ as the normal component of the displacement. The substrate induced piezoelectric potential scales with phonon displacement field u_L, while the deformation potential scales with iQu_L. Therefore, at low frequency, the more relevant mechanism is the interlayer coupling of electrons of graphene to the piezoelectric induced polarization in the substrate.

Acoustic deformation also generates a pseudogauge field $\boldsymbol{A}^{(\tau)}$ with $\tau = \pm$ indicating two time-reversal counterparts at two valleys with opposite chiralities. In order to comply with the overall time-reversal symmetry, such a gauge field requires opposite sign for two chiralities: $\boldsymbol{A}^{(\tau)} = \tau\boldsymbol{A} = \tau A_0(u_{xx} - u_{yy}, -2u_{xy})$ [27–34], where $A_0 = \hbar\beta/ea$, in which a is the lattice constant and the dimensionless parameter $\beta \sim 1$ is the Grüneisen's parameter indicating the strength of the electron-phonon coupling. Using Eq. (2) and neglecting second-order terms in u_z, the sound-induced dynamical vector potential reads

$$\boldsymbol{A}(\boldsymbol{r},t) = \tfrac{1}{2}(A_L\hat{\mathbf{Q}} + A_T\hat{\boldsymbol{\theta}})e^{i(\boldsymbol{Q}\cdot\boldsymbol{r}-\Omega t)} + \text{c.c.}, \tag{4}$$

where the vector potential is given in terms of longitudinal and transverse components $(A_L, A_T) = iA_0(Qu_L)(\cos(3\theta), -\sin(3\theta))$. Note that $\hat{\boldsymbol{\theta}} = \partial_\theta\hat{\boldsymbol{Q}}$ is the azimuthal unit vector transverse to $\hat{\boldsymbol{Q}}$ in the momentum space. Unlike the displacement field of the surface acoustic phonon, the sound-induced gauge field is not an elliptically polarized wave. The vector field stemming from the out-of-plane displacement is proportional to the u_z^2 due to $\partial_x h\partial_y h$, and therefore its impact on the AG current is less relevant.

The time- and space-dependent strain induces a scalar potential and pseudogauge field leading to the effective electromagnetic fields $\boldsymbol{E} = -\partial_{\boldsymbol{r}}V - \partial_t\boldsymbol{A}$ and $\boldsymbol{B} = \partial_{\boldsymbol{r}} \times \boldsymbol{A}$. In the second-order response to sound-induced fields, the acoustoelectric current or the rectification current formally follows

$$\mathcal{J}_\lambda^{(2)}(\boldsymbol{r},t) = \sum_\tau\sum_{\boldsymbol{q}_1,\boldsymbol{q}_2}\sum_{\omega_1,\omega_2}\sum_{\mu,\nu}\chi_{\lambda\mu\nu}^{(2)}(\boldsymbol{q}_1,\omega_1,\boldsymbol{q}_2,\omega_2) \times \mathcal{A}_\mu(\boldsymbol{q}_1,\omega_1)\mathcal{A}_\nu(\boldsymbol{q}_2,\omega_2)e^{-i(\omega_1+\omega_2)t}e^{i(\boldsymbol{q}_1+\boldsymbol{q}_2)\cdot\boldsymbol{r}}, \tag{5}$$

where $\chi_{\lambda\mu\nu}^{(2)}$ is the nonlinear acoustoelectric response function. Note that $\mathcal{J}^{(2)} = (n^{(2)}, \boldsymbol{j}^{(2)})$ is the four-vector of nonlinear density $n^{(2)}$ and current $\mathbf{j}^{(2)}$ and $\mathcal{A} = (V^{\mathrm{sc}}, \tau\boldsymbol{A}^{\mathrm{sc}})$ is an

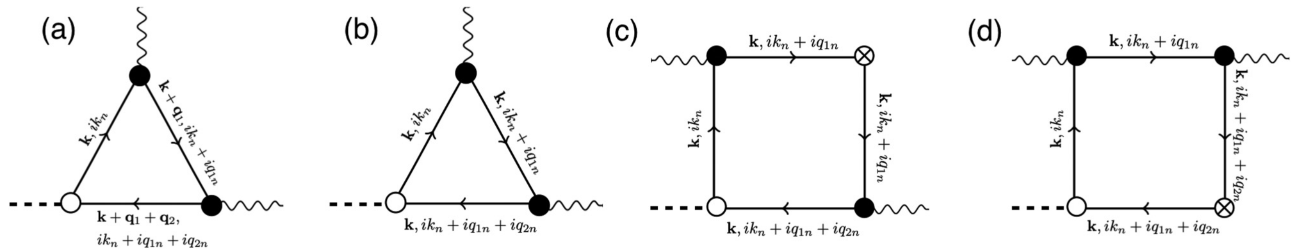

FIG. 2. Feynman diagrams for the acoustogalvanic response function in 2D hexagonal Dirac materials. (a) stands for the full nonlinear response function $\chi^{(2)}_{abc}$ with finite phonon wave vector $\boldsymbol{q}$. (b), (c), and (d) are the corresponding diagrams for X_{abc}, Y_{abdc}, and Z_{abcd} susceptibilities, respectively. Solid circles indicate the electron-phonon coupling vertex, and empty circles stand for the coupling of electrons to the electromagnetic (EM) fields (photons). Circles with a cross are for a current vertex with vanishing momentum and energy transfer to fermions. Wavy lines are external phonons, dashed lines are the output EM wave, and solid lines are the fermionic propagators with corresponding wave vector and Matsubara energies.

effective four-vector potential, where $V^{\rm sc}$ and $\boldsymbol{A}^{\rm sc}$ are the self-consistent sound-induced scalar and vector potentials, respectively. The second-order current generated by the interplay of scalar and vector potentials, $\tau V^{\rm sc}\boldsymbol{A}^{\rm sc}$, cancels out due to opposite contributions of two valleys $\tau = \pm$.

Diagrammatic theory of the nonlinear response function

We consider a 2D Dirac material whose low-energy Hamiltonian reads $\mathcal{H}(\mathbf{k}) = \hbar v_F(\tau k_x\sigma_x + k_y\sigma_y)$, where $\tau = \pm$ for the valley index (K, K'), v_F is the Fermi velocity, and σ_i's are the Pauli matrices in the pseudospin basis. The electron's coupling to the acoustic phonon thus is simply captured by setting $\hbar\boldsymbol{k} \to \hbar\boldsymbol{k} + e\tau\boldsymbol{A}(\boldsymbol{r}, t)$. Following the standard Kubo's formalism, the second-order current in the Dirac material can be obtained by evaluating the correlation function of three current operators $\hat{\mathbf{j}} = -(e/\hbar)\partial_{\mathbf{k}}\hat{\mathcal{H}} = -ev_F(\tau\hat{\sigma}_x, \hat{\sigma}_y)$. Accordingly, the nonlinear susceptibility reads [see the corresponding Feynman diagram in Fig. 2(a)]

$$\begin{aligned}\chi^{(2)}_{abc}(\boldsymbol{q}_1, iq_{1n}, \boldsymbol{q}_2, iq_{2n}) = \frac{1}{2}\sum_{\mathcal{P}}\frac{1}{S}\sum_{\boldsymbol{k}}\frac{1}{\beta}\sum_{ik_n}&\mathrm{tr}[\hat{j}_a\hat{G}(\boldsymbol{k}, ik_n)\hat{j}_b\\ &\times\hat{G}(\boldsymbol{k}+\boldsymbol{q}_1, ik_n + iq_{1n})\hat{j}_c\\ &\times\hat{G}(\boldsymbol{k}+\boldsymbol{q}_1+\boldsymbol{q}_2, ik_n+iq_{1n}+iq_{2n})],\end{aligned} \tag{6}$$

where $\hat{G}(\boldsymbol{k}, ik_n) = [ik_n - \hat{\mathcal{H}}(\boldsymbol{k})]^{-1}$ is the fermionic Green's function in the Matsubara frequency domain. Note that $\sum_{\mathcal{P}}$ stands for the intrinsic permutation symmetry for the exchange $(b, \boldsymbol{q}_1, iq_{1n}) \leftrightarrow (c, \boldsymbol{q}_2, iq_{2n})$, ik_n is the fermionic and iq_{in} is the bosonic (phononic) Matsubara energy, S is the area of the system, $\beta = 1/(k_BT)$ with T being the electronic temperature, and k_B is the Boltzmann constant. The trace operation tr[$\cdots$] sums over all discrete degrees of freedom such as spin, pseudospin, and valley indices. Performing the above summation over the fermion wave vector and keeping q finite is a formidable task. However, we proceed in a perturbative manner by expanding the Green's function up to the linear order in $\boldsymbol{q}$, the phonon wave vector:

$$\begin{aligned}\hat{G}(\boldsymbol{k}+\boldsymbol{q}, ik_n + iq_n) = {}&\hat{G}(\boldsymbol{k}, ik_n + iq_n)\\ &+\boldsymbol{q}\cdot\partial_{\boldsymbol{k}}\hat{G}(\boldsymbol{k}, ik_n + iq_n) + O(q^2).\end{aligned} \tag{7}$$

Using the relation $\hat{G}\hat{G}^{-1} = \hat{I}$ with $\hat{I}$ being the identity matrix, we have $\partial_{\boldsymbol{k}}\hat{G} = -\hat{G}\partial_{\boldsymbol{k}}\hat{G}^{-1}\hat{G}$. Therefore, by definition, we obtain

$$\partial_{k_a}\hat{G} = \hat{G}\left(-\frac{\hbar\hat{j}_a}{e}\right)\hat{G}. \tag{8}$$

Accordingly, we arrive at the following relation for the expansion of the Green's function:

$$\begin{aligned}\hat{G}(\boldsymbol{k}+\boldsymbol{q}, ik_n + iq_n) = {}&\hat{G}(\boldsymbol{k}, ik_n + iq_n)\\ &-\frac{\hbar}{e}\sum_a q_a\hat{G}(\boldsymbol{k}, ik_n + iq_n)\hat{j}_a\\ &\times\hat{G}(\boldsymbol{k}, ik_n + iq_n) + O(q^2).\end{aligned} \tag{9}$$

Utilizing the above equation, we expand the second-order response function up to leading order in $\boldsymbol{q}_i$:

$$\begin{aligned}&\chi^{(2)}_{abc}(\boldsymbol{q}_1, iq_{1n}, \boldsymbol{q}_2, iq_{2n})\\ &\approx\frac{1}{2}\sum_{\mathcal{P}}\Bigg\{X_{abc}(iq_{1n}, iq_{2n}) - \frac{\hbar}{e}\sum_d q_{1d}Y_{abdc}(iq_{1n}, iq_{2n})\\ &\quad-\frac{\hbar}{e}\sum_d(q_{1d}+q_{2d})Z_{abcd}(iq_{1n}, iq_{2n})\Bigg\},\end{aligned} \tag{10}$$

where X_{abc}, Y_{abdc}, and Z_{abcd} are diagrammatically depicted in Figs. 2(b)–2(d), respectively. In the following, we write the formal expressions of these correlation functions in terms of the Green's function $\hat{G}$ and the current operator $\hat{\mathbf{j}}$. The rank-3 tensor response function X_{abc} reads

$$\begin{aligned}&X_{abc}(iq_{1n}, iq_{2n})\\ &\quad=\frac{1}{S}\sum_{\boldsymbol{k}}\frac{1}{\beta}\sum_{ik_n}\mathrm{tr}[\hat{j}_a\hat{G}(\boldsymbol{k}, ik_n)\hat{j}_b\\ &\qquad\times\hat{G}(\boldsymbol{k}, ik_n + iq_{1n})\hat{j}_c\hat{G}(\boldsymbol{k}, ik_n + iq_{1n} + iq_{2n})].\end{aligned} \tag{11}$$

The rank-4 response function Y_{abdc} is given by

$$\begin{aligned}Y_{abdc}(iq_{1n}, iq_{2n}) = \frac{1}{S}\sum_{\boldsymbol{k}}\frac{1}{\beta}\sum_{ik_n}&\mathrm{tr}[\hat{j}_a\hat{G}(\boldsymbol{k}, ik_n)\hat{j}_b\\ &\times\hat{G}(\boldsymbol{k}, ik_n + iq_{1n})\hat{j}_d\hat{G}(\boldsymbol{k}, ik_n + iq_{1n})\hat{j}_c\\ &\times\hat{G}(\boldsymbol{k}, ik_n + iq_{1n} + iq_{2n})],\end{aligned} \tag{12}$$

and similarly the other rank-4 response function Z_{abcd} follows

$$\begin{aligned}
&Z_{abcd}(iq_{1n}, iq_{2n})\\
&\quad= \frac{1}{S}\sum_{\boldsymbol{k}}\frac{1}{\beta}\sum_{ik_n}\mathrm{tr}[\hat{j}_a\hat{G}(\boldsymbol{k}, ik_n)\hat{j}_b\\
&\qquad\times\hat{G}(\boldsymbol{k}, ik_n+iq_{1n})\hat{j}_c\hat{G}(\boldsymbol{k}, ik_n+iq_{1n}+iq_{2n})\hat{j}_d\\
&\qquad\times\hat{G}(\boldsymbol{k}, ik_n+iq_{1n}+iq_{2n})].
\end{aligned}\tag{13}$$

In inversion symmetric materials, any second-order homogeneous tensor vanishes identically. Therefore we have $X_{abc}=0$ in a gapless Dirac system. In centrosymmetric Dirac materials, the second-order nonlinear current is finite only with the nonlocal driving field wave vector ($\boldsymbol{q}\neq 0$). The wave vector associated with acoustic phonons is much larger than that of photons resulting in a stronger phonon-drag process compared with the photon-drag effect. In gapped Dirac materials such as gapped graphene and single-layer TMDs, the inversion symmetry is broken, and one can naturally expect a nonvanishing X_{abc} if it is not forbidden by rotational symmetries.

To evaluate the Y and Z response functions, we first perform the Matsubara summation on ik_n, and then we implement the analytical continuation $iq_{1n}\to\hbar\omega_1+i\delta$ and $iq_{2n}\to\hbar\omega_2+i\delta$ with $\delta\to 0^+$. Finally, we analytically evaluate the summation over fermion wave vector $\boldsymbol{k}$ in a continuum limit, $\sum_{\boldsymbol{k}}\to S\int d^2\boldsymbol{k}/(2\pi)^2$. The details of the derivation for the Y and Z response functions are given in Appendix A.

Following the perturbative treatment for long-wavelength sound waves, we can estimate the nonlinear response function in the leading order in phonon wave vector q_i

$$\begin{aligned}
\chi^{(2)}_{abc}(\boldsymbol{q}_1,\omega_1,\boldsymbol{q}_2,\omega_2) &= \frac{1}{2}\sum_d\{q_{1d}\gamma_{abcd}(\omega_1,\omega_2)\\
&\quad+q_{2d}\gamma_{acbd}(\omega_2,\omega_1)\}+O(q^2),
\end{aligned}\tag{14}$$

where γ_{abcd} is a local rank-4 tensor and is defined as

$$\begin{aligned}
\gamma_{abcd}(\omega_1,\omega_2) = -(\hbar/e)[&Y_{abdc}(\omega_1,\omega_2)+Z_{abcd}(\omega_1,\omega_2)\\
&+Z_{acbd}(\omega_2,\omega_1)].
\end{aligned}$$

Note that the second-order response function vanishes at the local approximation $q=0$ owing to the inversion symmetry of the isotropic gapless Dirac fermionic system. In addition, the above relation satisfies the intrinsic permutation symmetry [41] $\chi^{(2)}_{abc}(\boldsymbol{q}_1,\omega_1,\boldsymbol{q}_2,\omega_2)=\chi^{(2)}_{acb}(\boldsymbol{q}_2,\omega_2,\boldsymbol{q}_1,\omega_1)$. In the space-time domain, the second-order rectification current for the sound wave implies $\chi^{(2)}_{abc}(\boldsymbol{Q},\Omega,-\boldsymbol{Q},-\Omega)=[\chi^{(2)}_{abc}(-\boldsymbol{Q},-\Omega,\boldsymbol{Q},\Omega)]^*$, which leads to the property

$$\gamma_{abcd}(-\Omega,\Omega)=-\gamma^*_{abcd}(\Omega,-\Omega).\tag{15}$$

Therefore, with no need of explicit calculation, we expect the low-frequency scaling $\mathrm{Re}[\gamma_{abcd}(\Omega,-\Omega)]\sim\Omega$ and $\mathrm{Im}[\gamma_{abcd}(\Omega,-\Omega)]\sim 1$. Furthermore, for different spatial indices, there are 16 components of the rank-4 tensor quantities in the 2D Dirac system. Considering the isotropic symmetry of the Dirac Hamiltonian, there are just three nonvanishing independent tensor elements, namely, γ_{xxyy}, γ_{xyyx}, and γ_{xyxy}, and the remaining components can be expressed in terms of those, such as $\gamma_{xxxx}=\gamma_{xxyy}+\gamma_{xyxy}+\gamma_{xyyx}$ and other elements on interchanging $x\leftrightarrow y$. After straightforward algebraic calculations and following the Green's function technique, we obtain

$$\begin{aligned}
\gamma_{xxxx}(\omega_1,\omega_2) &= -\gamma_0\varepsilon_0\left\{\frac{1}{\hbar\omega_1}+\frac{1}{\hbar\omega_\Sigma}\right\}\mathrm{sgn}(\varepsilon_F)\\
&\quad\times\frac{4\varepsilon_F^4}{\big((\hbar\omega_1)^2-4\varepsilon_F^2\big)\big((\hbar\omega_\Sigma)^2-4\varepsilon_F^2\big)},
\end{aligned}\tag{16}$$

with $\gamma_0=N_f e^3 v_F^2/(\pi\hbar\varepsilon_0)$, where $N_f=4$ stands for the valley and spin degree of freedom and ε_0 is a unit of energy. The analytical expressions for other nonvanishing matrix elements of γ_{abcd}, i.e., γ_{xxyy}, γ_{xyxy}, and γ_{xyyx}, are given in Appendix B. Note that all frequencies contain an infinitesimal imaginary part, i.e., $\omega_i\equiv\omega_i+i0^+$, and ε_F is the Fermi energy. An apparent observation from this result is that the AE current changes sign and flows in the opposite direction in the electron and hole doped systems. Furthermore, this expression clearly states that the AE current vanishes when the Fermi energy approaches zero. These results are in agreement with experimental measurements of the AE effect in graphene [15,16,18]. The derived formulas are consistent with the literature for the light-induced nonlinear phenomenon [42–44].

In the following sections, we show that the acoustoelectric and acoustogalvanic currents can be expressed in terms of the $\gamma_{abcd}(\omega_1,\omega_2)$ response function and are induced by the scalar and vector potentials, respectively.

III. ACOUSTOELECTRIC CURRENT DUE TO SCALAR POTENTIALS

The rectified acoustoelectric current in response to the self-consistent scalar potential reads

$$j_a^{\mathrm{AE}}=\chi^{(2)}_{ann}(\boldsymbol{Q},\Omega,-\boldsymbol{Q},-\Omega)V^{\mathrm{sc}}(\boldsymbol{Q},\Omega)V^{\mathrm{sc}}(-\boldsymbol{Q},-\Omega),\tag{17}$$

where $\chi^{(2)}_{ann}$ is a current-density-density correlation function. The self-consistent potential is given as a summation of bare external potentials and the induced one owing to the long-range Coulomb interaction, i.e., *the screening effect*. For instance, up to the second-order perturbation, the self-consistent scalar potential reads

$$V^{\mathrm{sc}}(\boldsymbol{q},\omega)=V(\boldsymbol{q},\omega)+v_q\delta n^{(1)}(\boldsymbol{q},\omega)+v_q\delta n^{(2)}(\boldsymbol{q},\omega).\tag{18}$$

Here, $v_q=1/(2\epsilon_0\kappa q)$ is the Fourier transform of the Coulomb interaction in 2D, with ϵ_0 being the vacuum permittivity and κ being the dielectric constant of the surrounding environment [45]. Note that $\delta n^{(1)}$ and $\delta n^{(2)}$ are the linear and second-order density fluctuations, respectively. Following the standard random phase approximation (RPA) screening analysis, we obtain the self-consistent density response functions [44,46]

$$\delta n^{(1)}(\boldsymbol{q},\omega)=\chi^{(1)}_{nn}(\boldsymbol{q},\omega)V^{\mathrm{sc}}(\boldsymbol{q},\omega)\tag{19}$$

and

$$\begin{aligned}
\delta n^{(2)}(\boldsymbol{q},\omega) &= \sum_{\boldsymbol{q}_1,\boldsymbol{q}_2}\sum_{\omega_1,\omega_2}\chi^{(2)}_{nnn}(\boldsymbol{q}_1,\omega_1,\boldsymbol{q}_2,\omega_2)V^{\mathrm{sc}}(\boldsymbol{q}_1,\omega_1)\\
&\quad\times V^{\mathrm{sc}}(\boldsymbol{q}_2,\omega_2)\delta(\boldsymbol{q}-\boldsymbol{q}_\Sigma)\delta(\omega-\omega_\Sigma),
\end{aligned}\tag{20}$$

where $\chi^{(1)}_{nn}$ and $\chi^{(2)}_{nnn}$ stand for the first- and second-order density response functions. By plugging Eqs. (19) and (20) into Eq. (18), we obtain a self-consistent relation for $V^{\rm sc}$:

$$V^{\rm sc}(\boldsymbol{q},\omega)=\frac{V(\boldsymbol{q},\omega)}{\epsilon(\boldsymbol{q},\omega)}+\sum_{\boldsymbol{q}_1,\boldsymbol{q}_2}\sum_{\omega_1,\omega_2}\frac{v_q\chi^{(2)}_{nnn}(\boldsymbol{q}_1,\omega_1,\boldsymbol{q}_2,\omega_2)}{\epsilon(\boldsymbol{q},\omega)}\times V^{\rm sc}(\boldsymbol{q}_1,\omega_1)V^{\rm sc}(\boldsymbol{q}_2,\omega_2)\delta(\boldsymbol{q}-\boldsymbol{q}_\Sigma)\delta(\omega-\omega_\Sigma),\tag{21}$$

where $\boldsymbol{q}_\Sigma=\boldsymbol{q}_1+\boldsymbol{q}_2$ and $\omega_\Sigma=\omega_1+\omega_2$. Note that the dielectric function $\epsilon(\boldsymbol{q},\omega)=1-v_q\chi^{(1)}_{nn}(\boldsymbol{q},\omega)$ is given in terms of the linear density response function $\chi^{(1)}_{nn}$. In the absence of plasmon resonance at which the dielectric function vanishes, the first term in the above relation is dominant, and thus we neglect the nonlinear correction due to the second-order density response function. Therefore the rectified sound-induced scalar potential reads

$$V^{\rm sc}(\boldsymbol{Q},\Omega)V^{\rm sc}(-\boldsymbol{Q},-\Omega)\approx\frac{|V(\boldsymbol{Q},\Omega)|^2}{|\epsilon(\boldsymbol{Q},\Omega)|^2}.\tag{22}$$

The linear density response function is related to the longitudinal conductivity, i.e., $\chi^{(1)}_{nn}(\boldsymbol{q},\omega)=-i(q^2/\omega)\sigma(\boldsymbol{q},\omega)$ [45,47], and in the small-q limit the dielectric function simplifies to

$$\epsilon(\boldsymbol{q},\omega)\approx1+i\frac{v_sq}{\omega}\frac{\sigma(\omega)}{\sigma_m}.\tag{23}$$

The characteristic conductivity is given by $\sigma_m=2\epsilon_0\kappa v_s=\sigma_0(2\kappa/\pi\alpha)(v_s/c)$, with a conductivity unit $\sigma_0=e^2/4\hbar$ and $\alpha\approx1/137$ being the fine structure constant. Noting that $V(\boldsymbol{Q},\Omega)=(\Lambda_P-iQ\Lambda_D)u_L$, we find

$$j^{\rm AE}_a=\chi^{(2)}_{ann}(\boldsymbol{Q},\Omega,-\boldsymbol{Q},-\Omega)\frac{|V(\boldsymbol{Q},\Omega)|^2}{1+(\sigma/\sigma_m)^2}.\tag{24}$$

Using the gauge invariance arguments, the second-order response function (current-density-density) can be written in terms of the current-current-current correlation function as [47]

$$\chi_{ann}(\boldsymbol{Q},\Omega,-\boldsymbol{Q},-\Omega)=\sum_{bc}\frac{Q_bQ_c}{\Omega^2}\chi^{(2)}_{abc}(\boldsymbol{Q},\Omega,-\boldsymbol{Q},-\Omega),\tag{25}$$

where $\chi^{(2)}_{abc}\sim\langle\hat{j}_a\hat{j}_b\hat{j}_c\rangle$ is given as the correlation function of three current operators that is diagrammatically depicted in Fig. 2(a).

Specifically, the AE current in terms of the longitudinal and transverse basis can be decomposed as $\boldsymbol{j}^{\rm AE}=j^{\rm AE}_L\hat{\boldsymbol{Q}}+j^{\rm AE}_T\hat{\boldsymbol{\theta}}$. Accordingly, we require to know the nonlinear response function tensor elements in the longitudinal and transverse coordinates, for which we utilize $\chi^{(2)}_{abc}=\hat{\mathbf{e}}_a\cdot\chi^{(2)}:\hat{\mathbf{e}}_b\hat{\mathbf{e}}_c$ with $(\hat{\mathbf{e}}_L,\hat{\mathbf{e}}_T)=(\hat{\boldsymbol{Q}},\hat{\boldsymbol{\theta}})$. For the scalar potentials, the associated response will be $\chi^{(2)}_{aLL}$, where the last two indices are decided by the potential. The actual response in the small-q limit is dictated as $\chi^{(2)}_{aLL}\sim q_L\gamma_{aLLL}$. Accordingly, only the longitudinal component contributes to the AE current due to the finite γ_{LLLL} tensor element. Meanwhile, the transverse component γ_{TLLL} vanishes due to the mirror symmetry constraint of the 2D Dirac system. More explicitly, using Eq. (14) and the symmetry constraints of the γ_{abcd} tensor in the D$_6$ point group, we obtain $\chi^{(2)}_{TTT}=\chi^{(2)}_{TLL}=\chi^{(2)}_{LTL}=\chi^{(2)}_{LLT}=0$ and

$$\begin{aligned}\chi^{(2)}_{LLL}(\boldsymbol{Q},\Omega,\pm\boldsymbol{Q},-\Omega)&=Q\frac{\gamma_{xxxx}(\Omega,-\Omega)\pm\gamma_{xxxx}(-\Omega,\Omega)}{2},\\ \chi^{(2)}_{LTT}(\boldsymbol{Q},\Omega,\pm\boldsymbol{Q},-\Omega)&=Q\frac{\gamma_{xyyx}(\Omega,-\Omega)\pm\gamma_{xyyx}(-\Omega,\Omega)}{2},\\ \chi^{(2)}_{TLT}(\boldsymbol{Q},\Omega,\pm\boldsymbol{Q},-\Omega)&=Q\frac{\gamma_{xyxy}(\Omega,-\Omega)\pm\gamma_{xyxy}(-\Omega,\Omega)}{2},\\ \chi^{(2)}_{TTL}(\boldsymbol{Q},\Omega,\pm\boldsymbol{Q},-\Omega)&=\left[\chi^{(2)}_{TLT}(\boldsymbol{Q},\Omega,\pm\boldsymbol{Q},-\Omega)\right]^*.\end{aligned}\tag{26}$$

IV. LONGITUDINAL AND TRANSVERSE ACOUSTOGALVANIC CURRENT

For the current generated by the pseudogauge field (the AG current), the scenario of screening is completely different from the acoustoelectric current. This happens due to the strain-induced vector potential, having opposite signs in two different valleys that cannot generate a net charge current in the linear response [48]. Accordingly, the self-consistent pseudogauge field is equal to the external bare one: $\boldsymbol{A}^{\rm sc}=\boldsymbol{A}$. Therefore the rectified current induced by the pseudogauge field does *not* follow the conventional screening rule $\propto1/[1+(\sigma/\sigma_m)^2]$. In the rest of this section, we discuss the unscreened rectification current induced by the pseudogauge field, which we call "acoustogalvanic current."

For a monochromatic Rayleigh sound wave given by Eq. (2), we prove that the AG current reads

$$j^{(2)}_a(\boldsymbol{r})=j^{\rm AG}_a-2j^{\rm s-AG}_a\sin(2\boldsymbol{Q}\cdot\boldsymbol{r}),\tag{27}$$

where it consists of a uniform AG current component

$$j^{\rm AG}_a=\chi^{(2)}_{abc}(\boldsymbol{Q},\Omega,-\boldsymbol{Q},-\Omega)A_b(\boldsymbol{Q},\Omega)A^*_c(\boldsymbol{Q},\Omega),\tag{28}$$

as well as a spatially dispersive one

$$j^{\rm s-AG}_a=\chi^{(2)}_{abc}(\boldsymbol{Q},\Omega,\boldsymbol{Q},-\Omega)A_b(\boldsymbol{Q},\Omega)A^*_c(-\boldsymbol{Q},\Omega).\tag{29}$$

Here, the spatially dispersive AG current is a direct current induced by two counterpropagating surface acoustic waves that are spatially modulated with a vanishing net current after spatial integration. However, this modulation scales with the sound wavelength $\lambda_s=2\pi v_s/\Omega$ that is comparable to the typical source-drain distance $\ell_{\rm SD}\sim100\ \mu$m. In this context, this local current density can be practically probed in experiments. Similar dispersive current has been recently measured in the photogalvanic response of WTe$_2$ compounds [38,39]. By utilizing Eqs. (14) and (15), we simply find that $\chi^{(2)}_{abc}(\boldsymbol{Q},\Omega,-\boldsymbol{Q},-\Omega)=\sum_dQ_d{\rm Re}[\gamma_{abcd}(\Omega,-\Omega)]$ while $\chi^{(2)}_{abc}(\boldsymbol{Q},\Omega,\boldsymbol{Q},-\Omega)=i\sum_dQ_d{\rm Im}[\gamma_{abcd}(\Omega,-\Omega)]$. Afterward, using Eq. (26), we write the current components in the longitudinal and transverse coordinates. Accordingly, the uniform and spatially dispersive components of the AG currents are given by

$$j^{\rm AG}_{L,T}=j_0{\rm Re}[\Pi_{L,T}(\Omega,\varepsilon_F,\theta)]\tag{30}$$

and

$$j^{\rm s-AG}_{L,T}=j_0{\rm Im}[\Pi_{L,T}(\Omega,\varepsilon_F,\theta)],\tag{31}$$

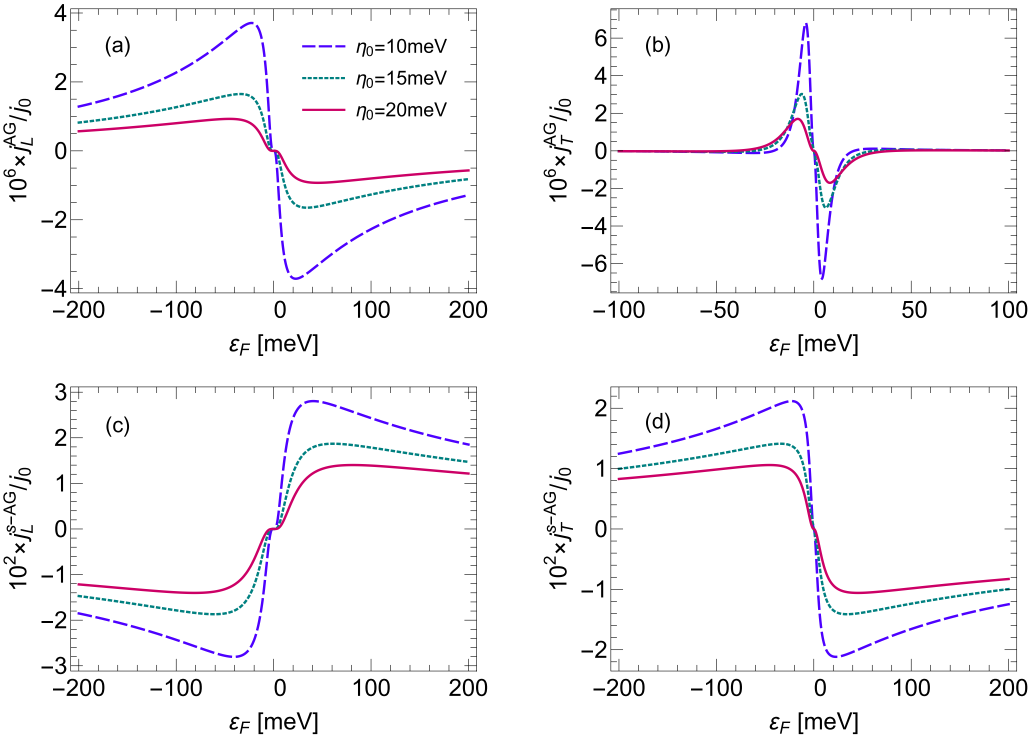

FIG. 3. Fermi energy dependence of the longitudinal and transverse components of the AG current in 2D hexagonal Dirac materials such as graphene. (a) and (b) indicate the longitudinal and transverse components of the uniform AG current, respectively. (c) and (d) illustrate the longitudinal and transverse components of the spatially dispersive AG current, respectively. We set $\theta = 0$ for the longitudinal and $\theta = \pi/12$ for the transverse current plots. The plots are made for the sound frequency $\Omega = 50$ MHz and the scattering rate $\eta = \eta_0 + 0.05|\varepsilon_F|$.

where the dimensionless parameters $\Pi_{L,T}$ are given as follows:

$$\Pi_L = \bar{\gamma}_{xxxx}(\Omega, -\Omega)\cos^2(3\theta) + \bar{\gamma}_{xyyx}(\Omega, -\Omega)\sin^2(3\theta) \tag{32}$$

and

$$\Pi_T = [\bar{\gamma}_{xyyx}(\Omega, -\Omega) - \bar{\gamma}_{xxxx}(\Omega, -\Omega)]\sin(6\theta), \tag{33}$$

where $\bar{\gamma}_{abcd} = \gamma_{abcd}/\gamma_0$ and $j_0 = \gamma_0 A_0^2 Q I_s/4I_0$. Note that the sound intensity is given by $I_s = I_0(Qu_L)^2$ with a characteristic 2D sound intensity $I_0 = \rho_{2\mathrm{D}} v_s^3$, where $\rho_{2\mathrm{D}}$ is the mass density of the 2D Dirac material. We should mention that the spatially dispersive (nonuniform) direct current can be also generated in response to the scalar potential; however, it will be screened and fully isotropic and longitudinal. We highlight Eqs. (30) and (31) as the central results of our work for the acoustogalvanic currents in 2D hexagonal Dirac materials. The two striking outcomes of our study are (i) the existence of a transverse component of the acoustogalvanic current and (ii) the existence of an anisotropic dispersive component of that current. (Both contributions are shown in Fig. 4 and discussed below.) We recall that the transverse AE current is absent in the conventional 2D electron gas [12].

V. NUMERICAL RESULTS AND DISCUSSION

Before presenting the quantitative results, it is worth highlighting four qualitative outcomes: (i) The AG current consists of both longitudinal and transverse components which depend on the direction of sound propagation θ. The longitudinal AG current is the sum of two contributions $j_1\cos^2(3\theta)$ and $j_2\sin^2(3\theta)$, while the transverse one scales as $j_3\sin(6\theta)$. (ii) The j_1 contribution stands for the longitudinal AG current that is driven by the longitudinal pseudogauge field A_L. The dynamical longitudinal vector potential describes a sound-induced pseudoelectric field $E \sim \Omega A_L$ that results in a rectification current $j_1 \sim EE^*$. (iii) The j_2 longitudinal current is driven by a transverse pseudogauge field A_T which describes a pseudomagnetic field $B \sim QA_T$ that results in a rectification current $j_2 \sim BB^*$. (iv) The j_3 transverse current is driven by the interference of the longitudinal and transverse components of the pseudogauge field ($j_3 \sim A_L A_T^* + \mathrm{c.c.}$) and thus scales as EB^*.

In Fig. 3, we illustrate the Fermi energy dependence of the different components of the AG current at the sound frequency $\Omega = 50$ MHz and at maximum angular variation $\theta = 0$ for the longitudinal component and $\theta = \pi/12$ for the transverse component. Note that the uniform AG current is proportional to the real part of Π, while the spatially dispersive AG current is proportional to the imaginary part of Π. An immediate observation is that the AG current has opposite signs in electron and hole doped systems: This is in agreement with experimental results [18]. By comparing Eq. (30) with Eq. (1), we notice that $\mathrm{Re}[\Pi_L] \propto \mu\Gamma_s$: Therefore the opposite sign of $\mathrm{Re}[\Pi_L]$ in electron and hole doped systems is consistent with the opposite signs of electron and hole mobility. A similar analogy works also for the spatial dispersive case,

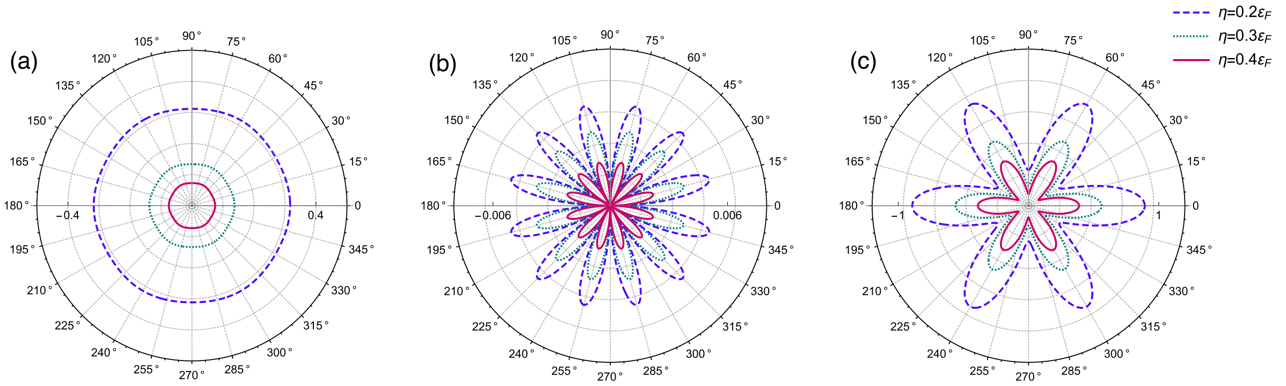

FIG. 4. Angular dependence of the longitudinal AG current components in 2D hexagonal Dirac materials. (a) Longitudinal AG current $10^6 \times j_L^{\rm AG}/j_0$, (b) transverse AG current $10^6 \times j_T^{\rm AG}/j_0$, and (c) spatially dispersive longitudinal AG current $10^2 \times j_L^{\rm AG}/j_0$. Note that the spatially dispersive transverse current $j_T^{\rm AG}$ holds the same anisotropic profile as in (b) but with stronger magnitude. As seen, the uniform longitudinal current is quite isotropic, while the transverse and specially dispersive current components are highly anisotropic. We set the Fermi energy $\varepsilon_F = 200$ meV and the sound frequency $\Omega = 50$ MHz.

for which the attenuation (dissipation) parameter is proportional to $\mathrm{Im}[\Pi_L]/\mu$. There are two Lorentzian maxima in the absolute value of $\mathrm{Re}[\Pi_L]$ and $\mathrm{Im}[\Pi_{L,T}]$ at the Fermi energy $\varepsilon_F \sim \pm\eta_0$. The case of $\mathrm{Re}[\Pi_T]$ is slightly different, and the maxima occur at $\varepsilon_F \sim \pm\eta_0/2$, where η is discussed below.

When the frequency is low, which is the case for sound waves, disorder must be taken into account, and therefore a many-body analysis of the nonlinear response function $\chi^{(2)}_{abc}$ is required. However, in the highly doped regime ($|\varepsilon_F| \gg \hbar\omega_i$), the disorder effect can be simply modeled by introducing a phenomenological relaxation rate η via the replacement $\omega_i \to \omega_i + i\eta$.

In principle, the relaxation rate depends on the Fermi energy, and the character of this dependence is different for different scattering mechanisms. At low temperature, impurity scattering is the dominant source of scattering. At large doping and for short-range impurity scattering we have $\eta \sim |\varepsilon_F|$, while for long-range scattering from charged impurities we get $\eta \sim 1/|\varepsilon_F|$ [49–54]. For instance, in the absence of charged impurity, we consider a more realistic phenomenological form $\eta = \eta_0 + g|\varepsilon_F|$, where η_0 is the constant relaxation rate at $\varepsilon_F = 0$ and g is a dimensionless parameter characterizing disorder scattering strength. At high doping $|\varepsilon_F| \gg \hbar\Omega$, the AG response function shows negative slope owing to the larger scattering rate η. Qualitatively, the longitudinal response drops as $\mathrm{Re}[\Pi_{L,T}] \sim 1/\eta^2 \sim 1/\varepsilon_F^2$ and $\mathrm{Im}[\Pi_{L,T}] \sim 1/\eta \sim 1/|\varepsilon_F|$.

The acoustogalvanic effect originates from the pseudogauge field, which inherits the threefold symmetry of the hexagonal lattice in 2D Dirac materials such as graphene and the TMD families. This threefold symmetry manifests itself in the angle-dependent factors in the second-order current in response to the sound-induced pseudogauge field. The transverse current is highly anisotropic and depends on the direction of propagation of the wave as $j_T \sim \sin(6\theta)$ regardless of other parameters. However, the longitudinal current contains two terms, $j_L \sim \sin^2(3\theta)$ and $j_L \sim \cos^2(3\theta)$, weighted by two different tensor elements of γ_{abcd}. In this regard, we depict the polar plots of longitudinal and transverse AG currents that illustrate the angular dependence of the sound propagation in Fig. 4. The uniform longitudinal AG current is almost isotropic as seen in Fig. 4(a) owing to the fact that the $\sin^2(3\theta)$ and $\cos^2(3\theta)$ terms contribute almost equally. However, the transverse AG current is highly anisotropic, consistent with $\sin(6\theta)$ dependence as is evident in Fig. 4(b). As seen in Fig. 4(c) the spatially dispersive longitudinal AG current is strongly anisotropic because the $\sin^2(3\theta)$ and $\cos^2(3\theta)$ terms contribute unequally.

Finally, we compare the amplitude of the AG current with the experimental measurements of conventional AE current in graphene [15,16,18,19]. For instance, the peak current ∼11 nA is measured at sound frequency $\Omega \sim 32$ MHz in a graphene device with the width ∼3 mm leading the AE current density $j_{\rm exp} \sim 3.6$ nA/mm [18]. The maximum sound intensity is reported to be $I_s \sim 0.3$ W/m [18]. We estimate the 2D mass density as $\rho_{\rm 2D} = d_{gr}\rho_{\rm 3D}$, where $\rho_{\rm 3D} = 2267$ kg/m^3 is the density of graphite and $d_{gr} \sim 1$ Å is the effective thickness of the graphene layer. With sound velocity $v_s \sim 4 \times 10^3$ m/s, we find $I_0 = \rho_{\rm 2D} v_s^3$, and therefore we obtain $I_s/I_0 \sim 2 \times 10^{-5}$. Accordingly, for $\beta \sim 3$, $v_F \sim 10^6$ m/s, and lattice constant $a \sim 0.246$ nm, we find $j_0 \sim 5 \times 10^6$ nA/mm. For $\theta = 0$ (i.e., for a sound wave propagating in the zigzag direction), with Fermi energy $\varepsilon_F \sim 50$ meV and scattering rate $\eta \sim 20$ meV, we evaluate Π_L, and then we estimate the uniform longitudinal AG currents $|j_L^{\rm AG}| \sim 3$ nA/mm. Thus the calculated uniform AG current $j_L^{\rm AG}$ is on the order of the measured value.

VI. SUMMARY

We have discussed the acoustogalvanic (AG) effect in 2D hexagonal Dirac materials using the Kubo's formalism. Apart from the self-consistently screened deformation potential, sound propagation in Dirac materials induces pseudo electromagnetic fields which are not subject to screening. We have analyzed both the uniform and the spatially dispersive components of the AG current. We identify an anisotropic uniform current transverse to the sound propagation direction and a highly anisotropic profile of the spatial dispersive AG currents. The AG response changes sign in going from electron to hole doped systems, which is consistent with expectations for the standard AE effect. While our calculations have been performed for graphene, our formalism can be easily adapted to other 2D materials such as transition metal dichalcogenides and their heterostructures. Furthermore, our results provide a direction to design future experiments to explore fundamental aspects as well as applications of transverse and spatially dispersive acoustoelectric currents in graphene.

ACKNOWLEDGMENTS

This work was supported by Nordita and the Swedish Research Council (VR 2018-04252). Nordita is supported in part by Nordforsk. We thank E. Cappelluti for carefully reading the manuscript and useful comments.

APPENDIX A: DETAILED CALCULATION OF γ_{abcd} TENSOR ELEMENTS USING KUBO'S FORMALISM

1. Calculation for the Y_{abdc} quantity

According to Eq. (12), the fourth-rank tensor quantity Y_{abdc} is given by [see the Feynman diagram in Fig. 2(c)]

$$Y_{abdc}(iq_{1n}, iq_{2n}) = \frac{1}{S}\sum_{\boldsymbol{k}}\frac{1}{\beta}\sum_{ik_n}\mathrm{tr}[\hat{j}_a\hat{G}(\boldsymbol{k}, ik_n)\hat{j}_b\hat{G}(\boldsymbol{k}, ik_n+iq_{1n})\hat{j}_d\hat{G}(\boldsymbol{k}, ik_n+iq_{1n})\hat{j}_c\hat{G}(\boldsymbol{k}, ik_n+iq_{1n}+iq_{2n})], \tag{A1}$$

where $\hat{j}$ is the current vertex, $\hat{G}$ is the fermionic Green's function, and β refers to the inverse of the temperature. To find the solution, it is convenient to express the equation in the band basis which is represented by $|\boldsymbol{k}, \lambda\rangle$, where $\lambda \equiv \pm$ having $(+)$ sign for the conduction band and $(-)$ sign for the valence band. Using the relations,

$$\langle\lambda_i|\hat{j}_\alpha|\lambda_j\rangle = j_\alpha^{\lambda_i\lambda_j}, \quad \langle\lambda_i|\hat{G}|\lambda_j\rangle = \frac{\delta_{\lambda_i\lambda_j}}{ik_n - \varepsilon_{\boldsymbol{k}}^{\lambda_i}}. \tag{A2}$$

Here, the band dispersion for the 2D Dirac material is $\varepsilon_{\mathbf{k}}^{\lambda} = \lambda\hbar v_F|\boldsymbol{k}|$, where $\lambda = \pm$ for the conduction and valence bands and v_F is the Fermi velocity. Considering Eq. (A2), we rewrite the tensor quantity in Eq. (A1) as follows:

$$Y_{abdc}(iq_{1n}, iq_{2n}) = \frac{1}{S}\sum_{\mathbf{k}}\frac{1}{\beta}\sum_{ik_n}\sum_{\lambda_i=\pm} j_a^{\lambda_1\lambda_2} j_b^{\lambda_2\lambda_3} j_d^{\lambda_3\lambda_4} j_c^{\lambda_4\lambda_1}\frac{1}{ik_n - \varepsilon_{\boldsymbol{k}}^{\lambda_2}}\frac{1}{ik_n + iq_{1,n} - \varepsilon_{\boldsymbol{k}}^{\lambda_3}}\frac{1}{ik_n + iq_{1,n} - \varepsilon_{\boldsymbol{k}}^{\lambda_4}}\frac{1}{ik_n + iq_{1,n} + iq_{2,n} - \varepsilon_{\boldsymbol{k}}^{\lambda_1}}. \tag{A3}$$

To stratify it further, first we perform the Matsubara summations over the Green's functions, which give

$$\begin{aligned} Y_{abdc}(\omega_1, \omega_2) = \frac{1}{S}\sum_{\mathbf{k}}\frac{1}{\beta}\sum_{\lambda_i=\pm}\frac{j_a^{\lambda_1\lambda_2} j_b^{\lambda_2\lambda_3} j_d^{\lambda_3\lambda_4} j_c^{\lambda_4\lambda_1}}{\omega_1 + \omega_2 - \varepsilon_{\boldsymbol{k}}^{\lambda_1\lambda_2}}\Bigg\{&\frac{1}{\omega_1 - \varepsilon_{\boldsymbol{k}}^{\lambda_4\lambda_2}}\left(\frac{n_F(\varepsilon_{\boldsymbol{k}}^{\lambda_2}) - n_F(\varepsilon_{\boldsymbol{k}}^{\lambda_3})}{\omega_1 - \varepsilon_{\boldsymbol{k}}^{\lambda_3\lambda_2}} + \frac{n_F(\varepsilon_{\boldsymbol{k}}^{\lambda_3}) - n_F(\varepsilon_{\boldsymbol{k}}^{\lambda_4})}{\varepsilon_{\boldsymbol{k}}^{\lambda_4\lambda_3}}\right) \\ &+ \frac{1}{\omega_2 - \varepsilon_{\boldsymbol{k}}^{\lambda_1\lambda_4}}\left(\frac{n_F(\varepsilon_{\boldsymbol{k}}^{\lambda_3}) - n_F(\varepsilon_{\boldsymbol{k}}^{\lambda_4})}{\varepsilon_{\boldsymbol{k}}^{\lambda_4\lambda_3}} + \frac{n_F(\varepsilon_{\boldsymbol{k}}^{\lambda_3}) - n_F(\varepsilon_{\boldsymbol{k}}^{\lambda_1})}{\omega_2 - \varepsilon_{\boldsymbol{k}}^{\lambda_1\lambda_3}}\right)\Bigg\}, \end{aligned} \tag{A4}$$

where $n_F(x) = [e^{\beta(x-\mu)} + 1]^{-1}$ is the Fermi-Dirac distribution function and $\varepsilon_{\boldsymbol{k}}^{\lambda_i\lambda_j} = \varepsilon_{\boldsymbol{k}}^{\lambda_i} - \varepsilon_{\boldsymbol{k}}^{\lambda_j}$ is the difference between the dispersions of two bands. It is to be noted that we here use the shorthand notation $iq_{j,n} = \omega_j + i\delta = \omega_j$. Now, we will calculate the tensor quantities for different combinations of the Cartesian indices. First, the conductivity tensor $Y_{xxyy}(\omega_1, \omega_2)$ is given by

$$\begin{aligned} Y_{xxyy}(\omega_1, \omega_2) = \frac{1}{S}\sum_{\mathbf{k}}\frac{1}{\beta}\sum_{\lambda_i=\pm}\frac{\mathcal{F}_{xxyy}^{1234}}{\omega_1 + \omega_2 - \varepsilon_{\boldsymbol{k}}^{\lambda_1\lambda_2}}\Bigg\{&\frac{1}{\omega_1 - \varepsilon_{\boldsymbol{k}}^{\lambda_4\lambda_2}}\left(\frac{n_F(\varepsilon_{\boldsymbol{k}}^{\lambda_2}) - n_F(\varepsilon_{\boldsymbol{k}}^{\lambda_3})}{\omega_1 - \varepsilon_{\boldsymbol{k}}^{\lambda_3\lambda_2}} + \frac{n_F(\varepsilon_{\boldsymbol{k}}^{\lambda_3}) - n_F(\varepsilon_{\boldsymbol{k}}^{\lambda_4})}{\varepsilon_{\boldsymbol{k}}^{\lambda_4\lambda_3}}\right) \\ &+ \frac{1}{\omega_2 - \varepsilon_{\boldsymbol{k}}^{\lambda_1\lambda_4}}\left(\frac{n_F(\varepsilon_{\boldsymbol{k}}^{\lambda_3}) - n_F(\varepsilon_{\boldsymbol{k}}^{\lambda_4})}{\varepsilon_{\boldsymbol{k}}^{\lambda_4\lambda_3}} + \frac{n_F(\varepsilon_{\boldsymbol{k}}^{\lambda_3}) - n_F(\varepsilon_{\boldsymbol{k}}^{\lambda_1})}{\omega_2 - \varepsilon_{\boldsymbol{k}}^{\lambda_1\lambda_3}}\right)\Bigg\}, \end{aligned} \tag{A5}$$

where $\mathcal{F}_{xxyy}^{1234} = j_x^{\lambda_1\lambda_2} j_x^{\lambda_2\lambda_3} j_y^{\lambda_3\lambda_4} j_y^{\lambda_4\lambda_1}$ is the form factor. The latter quantity is only a function of angle and is independent of the wave vector; thus on performing the angular integration we get

$$\begin{aligned} \int_0^{2\pi} d\theta\mathcal{F}_{xxyy}^{1234} &= \int_0^{2\pi} d\theta\frac{\lambda_1 e^{-i\tau\phi(\boldsymbol{k})} + \lambda_2 e^{i\tau\phi(\boldsymbol{k})}}{2}\frac{\lambda_2 e^{-i\tau\phi(\boldsymbol{k})} + \lambda_3 e^{i\tau\phi(\boldsymbol{k})}}{2}\frac{\lambda_3 e^{-i\tau\phi(\boldsymbol{k})} - \lambda_4 e^{i\tau\phi(\boldsymbol{k})}}{2}\frac{\lambda_4 e^{-i\tau\phi(\boldsymbol{k})} - \lambda_1 e^{i\tau\phi(\boldsymbol{k})}}{2} \\ &= \frac{\pi}{4}(1 - \lambda_2\lambda_4 + \lambda_1\lambda_3). \end{aligned} \tag{A6}$$

It is evident from the expression for $Y_{xxyy}(\omega_1, \omega_2)$ that the quantity will yield a strong contribution for the degenerate case $\lambda_3 = \lambda_4$. For this case, the integration over the wave vector and the summation over the band indices reduce the tensor quantity in the form

$$Y_{xxyy}(\omega_1,\omega_2)=\mathrm{sgn}(\varepsilon_F)\frac{e^4v_F^2}{8\pi\hbar^2}\frac{16\varepsilon_F^2\big(-\omega_1\omega_2^2+\varepsilon_F^2(3\omega_1+\omega_2)\big)}{\omega_1\omega_2\big(\omega_1^2-4\varepsilon_F^2\big)\big(\omega_2^2-4\varepsilon_F^2\big)}. \tag{A7}$$

Similarly, the other elements give

$$Y_{xyyx}(\omega_1,\omega_2)=\frac{e^4v_F^2}{8\pi\hbar^2}\frac{\mathrm{sgn}(\varepsilon_F)16\varepsilon_F^2(\omega_2-\omega_1)\big(\omega_1\omega_2+\varepsilon_F^2\big)}{\omega_1\omega_2\big(\omega_1^2-4\varepsilon_F^2\big)\big(\omega_2^2-4\varepsilon_F^2\big)}, \tag{A8}$$

$$Y_{xyxy}(\omega_1,\omega_2)=\frac{e^4v_F^2}{8\pi\hbar^2}\frac{\mathrm{sgn}(\varepsilon_F)16\varepsilon_F^2\big(\omega_1^2\omega_2-\varepsilon_F^2(\omega_1+3\omega_2)\big)}{\omega_1\omega_2\big(\omega_1^2-4\varepsilon_F^2\big)\big(\omega_2^2-4\varepsilon_F^2\big)}. \tag{A9}$$

2. Calculation for the Z_{abcd} quantity

The rank-4 quantity Z_{abcd} corresponds to the Feynman diagram in Fig. 2(d) and can be written as

$$Z_{abcd}(iq_{1n},iq_{2n})=\frac{1}{S}\sum_{\mathbf{k}}\frac{1}{\beta}\sum_{ik_n}\sum_{\lambda_i=\pm}\mathrm{tr}[\hat{j}_a\hat{G}(\mathbf{k},ik_n)\hat{j}_b\hat{G}(\mathbf{k},ik_n+iq_{1n})\hat{j}_c\hat{G}(\mathbf{k},ik_n+iq_{1n}+iq_{2n})\hat{j}_d\hat{G}(\mathbf{k},ik_n+iq_{1n}+iq_{2n})]. \tag{A10}$$

In the band basis representation, it becomes

$$\begin{aligned}Z_{abcd}(iq_{1n},iq_{2n})=&\frac{1}{S}\sum_{\mathbf{k}}\frac{1}{\beta}\sum_{ik_n}\sum_{\lambda_i=\pm}j_a^{\lambda_1\lambda_2}j_b^{\lambda_2\lambda_3}j_c^{\lambda_3\lambda_4}j_d^{\lambda_4\lambda_1}\\&\times\frac{1}{ik_n-\varepsilon_{\boldsymbol{k}}^{\lambda_2}}\frac{1}{ik_n+iq_{1,n}-\varepsilon_{\boldsymbol{k}}^{\lambda_3}}\frac{1}{ik_n+iq_{1,n}+iq_{2,n}-\varepsilon_{\boldsymbol{k}}^{\lambda_4}}\frac{1}{ik_n+iq_{1,n}+iq_{2,n}-\varepsilon_{\boldsymbol{k}}^{\lambda_1}}.\end{aligned} \tag{A11}$$

Performing the Matsubara frequency summations and then doing the analytic continuation, we obtain

$$\begin{aligned}Z_{abcd}(\omega_1,\omega_2)=&\frac{1}{S}\sum_{\mathbf{k}}\sum_{\lambda_i=\pm}\frac{j_a^{\lambda_1\lambda_2}j_b^{\lambda_2\lambda_3}j_c^{\lambda_3\lambda_4}j_d^{\lambda_4\lambda_1}}{(\omega_1-\varepsilon_{\boldsymbol{k}}^{\lambda_3\lambda_2})\varepsilon_{\boldsymbol{k}}^{\lambda_1\lambda_4}}\left\{\frac{n_F(\varepsilon_{\boldsymbol{k}}^{\lambda_4})-n_F(\varepsilon_{\boldsymbol{k}}^{\lambda_2})}{\omega_1+\omega_2-\varepsilon_{\boldsymbol{k}}^{\lambda_4\lambda_2}}-\frac{n_F(\varepsilon_{\boldsymbol{k}}^{\lambda_4})-n_F(\varepsilon_{\boldsymbol{k}}^{\lambda_3})}{\omega_2-\varepsilon_{\boldsymbol{k}}^{\lambda_4\lambda_3}}\right.\\&\left.+\frac{n_F(\varepsilon_{\boldsymbol{k}}^{\lambda_1})-n_F(\varepsilon_{\boldsymbol{k}}^{\lambda_3})}{\omega_2-\varepsilon_{\boldsymbol{k}}^{\lambda_1\lambda_3}}-\frac{n_F(\varepsilon_{\boldsymbol{k}}^{\lambda_1})-n_F(\varepsilon_{\boldsymbol{k}}^{\lambda_2})}{\omega_1+\omega_2-\varepsilon_{\boldsymbol{k}}^{\lambda_1\lambda_2}}\right\}.\end{aligned} \tag{A12}$$

For different spatial indices combinations, this expression reduces to the following forms:

$$Z_{xxyy}(\omega_1,\omega_2)=\mathrm{sgn}(\varepsilon_F)\frac{e^4v_F^2}{8\pi\hbar^2}\frac{16\varepsilon_F^2\big(\omega_\Sigma\omega_2^2-\varepsilon_F^2(3\omega_1+2\omega_2)\big)}{\omega_2\omega_\Sigma\big(\omega_\Sigma^2-4\varepsilon_F^2\big)\big(\omega_2^2-4\varepsilon_F^2\big)}, \tag{A13}$$

$$Z_{xyyx}(\omega_1,\omega_2)=\frac{e^4v_F^2}{8\pi\hbar^2}\frac{\mathrm{sgn}(\varepsilon_F)16\varepsilon_F^2\big(\omega_2\omega_\Sigma^2+\varepsilon_F^2(\omega_1-2\omega_2)\big)}{\omega_2\omega_\Sigma\big(\omega_\Sigma^2-4\varepsilon_F^2\big)\big(\omega_2^2-4\varepsilon_F^2\big)}, \tag{A14}$$

$$Z_{xyxy}(\omega_1,\omega_2)=\frac{e^4v_F^2}{8\pi\hbar^2}\frac{\mathrm{sgn}(\varepsilon_F)16\varepsilon_F^2(\omega_1+2\omega_2)\big(\varepsilon_F^2-\omega_2\omega_\Sigma\big)}{\omega_2\omega_\Sigma\big(\omega_\Sigma^2-4\varepsilon_F^2\big)\big(\omega_2^2-4\varepsilon_F^2\big)}. \tag{A15}$$

APPENDIX B: EXPLICIT EXPRESSIONS OF γ_{xxyy}, γ_{xyyx}, AND γ_{xyxy}

The different forms of the fourth-rank tensor quantity which is defined in the form $\gamma_{abcd}(\omega_1,\omega_2)=-(\hbar/e)[Y_{abdc}(\omega_1,\omega_2)+Z_{abcd}(\omega_1,\omega_2)+Z_{acbd}(\omega_2,\omega_1)]$ are listed below:

$$\gamma_{xxyy}(\omega_1,\omega_2)=\gamma_0\frac{4\varepsilon_0\mathrm{sgn}(\varepsilon_F)\varepsilon_F^2(2\hbar\omega_1+\hbar\omega_2)\big(\varepsilon_F^2-\hbar\omega_1\hbar\omega_\Sigma\big)}{\hbar\omega_1\hbar\omega_\Sigma\big((\hbar\omega_1)^2-4\varepsilon_F^2\big)\big((\hbar\omega_\Sigma)^2-4\varepsilon_F^2\big)}, \tag{B1}$$

$$\gamma_{xyyx}(\omega_1,\omega_2)=\gamma_0\frac{2\varepsilon_0\mathrm{sgn}(\varepsilon_F)\varepsilon_F^2\big(8\varepsilon_F^4\hbar\omega_2+\varepsilon_F^2\hbar^3\big(4\omega_1^3+8\omega_1^2\omega_2+4\omega_1\omega_2^2-2\omega_2^3\big)-\hbar^5\omega_1\omega_\Sigma\big(2\omega_1^3+3\omega_1^2\omega_2-2\omega_1\omega_2^2-\omega_2^3\big)\big)}{\hbar\omega_1\hbar\omega_\Sigma\big((\hbar\omega_1)^2-4\varepsilon_F^2\big)\big((\hbar\omega_2)^2-4\varepsilon_F^2\big)\big((\hbar\omega_\Sigma)^2-4\varepsilon_F^2\big)}, \tag{B2}$$

and

$$\gamma_{xyxy}(\omega_1,\omega_2)=\gamma_0\frac{2\varepsilon_0\mathrm{sgn}(\varepsilon_F)\varepsilon_F^2\big(8\varepsilon_F^4\hbar(4\omega_1+\omega_2)-2\varepsilon_F^2\hbar^3\big[10\omega_1\big(\omega_1^2+\omega_2^2\big)+16\omega_2\omega_1^2+\omega_2^3\big]+\hbar^5\omega_1\omega_\Sigma^2\big(2\omega_1^2+\omega_2^2+\omega_1\omega_2\big)\big)}{\hbar\omega_1\hbar\omega_\Sigma\big((\hbar\omega_1)^2-4\varepsilon_F^2\big)\big((\hbar\omega_2)^2-4\varepsilon_F^2\big)\big((\hbar\omega_\Sigma)^2-4\varepsilon_F^2\big)}. \tag{B3}$$

[1] R. H. Parmenter, The acousto-electric effect, Phys. Rev. **89**, 990 (1953).

[2] G. Weinreich, Ultrasonic attenuation by free carriers in germanium, Phys. Rev. **107**, 317 (1957).

[3] G. Weinreich and H. G. White, Observation of the acoustoelectric effect, Phys. Rev. **106**, 1104 (1957).

[4] W. Sasaki and E. Yoshida, Acoustoelectric effect in n-type germanium, J. Phys. Soc. Jpn. **12**, 979A (1957).

[5] G. Weinreich, T. M. Sanders, and H. G. White, Acoustoelectric effect in n-type germanium, Phys. Rev. **114**, 33 (1959).

[6] P. Smith and D. O. Sproule, Experiments on the acousto-electric effect, Nature (London) **184**, 264 (1959).

[7] S. G. Eckstein, Acoustoelectric effect, J. Appl. Phys. (Melville, NY) **35**, 2702 (1964).

[8] R. L. Willett, M. A. Paalanen, R. R. Ruel, K. W. West, L. N. Pfeiffer, and D. J. Bishop, Anomalous Sound Propagation at $\nu = 1/2$ in a 2D Electron Gas: Observation of a Spontaneously Broken Translational Symmetry? Phys. Rev. Lett. **65**, 112 (1990).

[9] Y. Ilisavskii, A. Goltsev, K. Dyakonov, V. Popov, E. Yakhkind, V. P. Dyakonov, P. Gierłowski, A. Klimov, S. J. Lewandowski, and H. Szymczak, Anomalous Acoustoelectric Effect in $La_{0.67}Ca_{0.33}MnO_3$ Films, Phys. Rev. Lett. **87**, 146602 (2001).

[10] K. Gloos, P. Utko, J. B. Hansen, and P. E. Lindelof, Quantized acoustoelectric current in the presence of large tunneling counterflow, Phys. Rev. B **70**, 235345 (2004).

[11] D. J. Kreft, L. G. Mourokh, H. Shin, M. Bichler, W. Wegscheider, and R. H. Blick, Giant acoustoelectric current in suspended quantum point contacts, Phys. Rev. B **94**, 235305 (2016).

[12] V. I. Fal'ko, S. V. Meshkov, and S. V. Iordanskii, Acoustoelectric drag effect in the two-dimensional electron gas at strong magnetic field, Phys. Rev. B **47**, 9910 (1993).

[13] S. H. Simon, Coupling of surface acoustic waves to a two-dimensional electron gas, Phys. Rev. B **54**, 13878 (1996).

[14] V. Miseikis, J. E. Cunningham, K. Saeed, R. O'Rorke, and A. G. Davies, Acoustically induced current flow in graphene, Appl. Phys. Lett. **100**, 133105 (2012).

[15] L. Bandhu, L. M. Lawton, and G. R. Nash, Macroscopic acoustoelectric charge transport in graphene, Appl. Phys. Lett. **103**, 133101 (2013).

[16] L. Bandhu and G. R. Nash, Temperature dependence of the acoustoelectric current in graphene, Appl. Phys. Lett. **105**, 263106 (2014).

[17] S. Zheng, H. Zhang, Z. Feng, Y. Yu, R. Zhang, C. Sun, J. Liu, X. Duan, W. Pang, and D. Zhang, Acoustic charge transport induced by the surface acoustic wave in chemical doped graphene, Appl. Phys. Lett. **109**, 183110 (2016).

[18] L. Bandhu and G. R. Nash, Controlling the properties of surface acoustic waves using graphene, Nano Research **9**, 685 (2016).

[19] T. Poole and G. R. Nash, Acoustoelectric current in graphene nanoribbons, Sci. Rep. **7**, 1767 (2017).

[20] K. A. Ingebrigtsen, Linear and nonlinear attenuation of acoustic surface waves in a piezoelectric coated with a semiconducting film, J. Appl. Phys. (Melville, NY) **41**, 454 (1970).

[21] *Nonlinear Waves in Solid State Physics*, edited by A. D. Boardman, M. Bertolotti, and T. Twardowski, NATO ASI Series B, Vol. 247 (Springer, New York, 1990).

[22] There is an inconsistency in the literature, e.g., Refs. [20,21], for the overall minus sign in Eq. (1) that can be due to a different convention for the coordinate.

[23] A. Wixforth, J. P. Kotthaus, and G. Weimann, Quantum Oscillations in the Surface-Acoustic-Wave Attenuation Caused by a Two-Dimensional Electron System, Phys. Rev. Lett. **56**, 2104 (1986).

[24] G. D. Mahan, *Many-Body Physics* (Kluwer, New York, 2000).

[25] A Hernández-Mínguez, Y.-T. Liou, and P. V. Santos, Interaction of surface acoustic waves with electronic excitations in graphene, J. Phys. D: Appl. Phys. **51**, 383001 (2018).

[26] A. V. Kalameitsev, V. M. Kovalev, and I. G. Savenko, Valley Acoustoelectric Effect, Phys. Rev. Lett. **122**, 256801 (2019).

[27] C. L. Kane and E. J. Mele, Size, Shape, and Low Energy Electronic Structure of Carbon Nanotubes, Phys. Rev. Lett. **78**, 1932 (1997).

[28] H. Suzuura and T. Ando, Phonons and electron-phonon scattering in carbon nanotubes, Phys. Rev. B **65**, 235412 (2002).

[29] K.-i. Sasaki, Y. Kawazoe, and R. Saito, Local energy gap in deformed carbon nanotubes, Prog. Theor. Phys. **113**, 463 (2005).

[30] M. I. Katsnelson and K. S. Novoselov, Graphene: New bridge between condensed matter physics and quantum electrodynamics, Solid State Commun. **143**, 3 (2007).

[31] F. Guinea, M. I. Katsnelson, and A. K. Geim, Energy gaps and a zero-field quantum Hall effect in graphene by strain engineering, Nat. Phys. **6**, 30 (2010).

[32] M. A. H. Vozmediano, M. I. Katsnelson, and F. Guinea, Gauge fields in graphene, Phys. Rep. **496**, 109 (2010).

[33] H. Rostami and R. Asgari, Electronic structure and layer-resolved transmission of bilayer graphene nanoribbon in the presence of vertical fields, Phys. Rev. B **88**, 035404 (2013).

[34] H. Rostami, R. Roldán, E. Cappelluti, R. Asgari, and F. Guinea, Theory of strain in single-layer transition metal dichalcogenides, Phys. Rev. B **92**, 195402 (2015).

[35] H. Rostami, F. Guinea, M. Polini, and R. Roldán, Piezoelectricity and valley Chern number in inhomogeneous hexagonal 2D crystals, npj 2D Mater. Appl. **2**, 15 (2018).

[36] P. O. Sukhachov and H. Rostami, Acoustogalvanic Effect in Dirac and Weyl Semimetals, Phys. Rev. Lett. **124**, 126602 (2020).

[37] L. Liang, P. O. Sukhachov, and A. V. Balatsky, Axial Magnetoelectric Effect in Dirac Semimetals, Phys. Rev. Lett. **126**, 247202 (2021).

[38] Z. Ji, G. Liu, Z. Addison, W. Liu, P. Yu, H. Gao, Z. Liu, A. M. Rappe, C. L. Kane, E. J. Mele, and R. Agarwal, Spatially dispersive circular photogalvanic effect in a Weyl semimetal, Nat. Mater. **18**, 955 (2019).

[39] Z. Ji, W. Liu, S. Krylyuk, X. Fan, Z. Zhang, A. Pan, L. Feng, A. Davydov, and R. Agarwal, Photocurrent detection of the orbital angular momentum of light, Science **368**, 763 (2020).

[40] S. V. Biryukov, S. V. Biriukov, Y. V. Gulyaev, V. V. Krylov, and V. P. Plessky, *Surface Acoustic Waves in Inhomogeneous Media*, Springer Series on Wave Phenomena Vol. 20 (Springer, Berlin, 1995).

[41] P. N. Butcher and D. Cotter, *The Elements of Nonlinear Optics*, Cambridge Studies in Modern Optics Vol. 9 (Cambridge University Press, Cambridge, UK, 1990).

[42] Y. Wang, M. Tokman, and A. Belyanin, Second-order nonlinear optical response of graphene, Phys. Rev. B **94**, 195442 (2016).

[43] J. L. Cheng, N. Vermeulen, and J. E. Sipe, Second order optical nonlinearity of graphene due to electric quadrupole and magnetic dipole effects, Sci. Rep. **7**, 43843 (2017).

[44] H. Rostami, M. I. Katsnelson, and M. Polini, Theory of plasmonic effects in nonlinear optics: The case of graphene, Phys. Rev. B **95**, 035416 (2017).

[45] G. F. Giuliani and G. Vignale, *Quantum Theory of the Electron Liquid* (Cambridge University Press, Cambridge, UK, 2005).

[46] S. A. Mikhailov, Theory of the giant plasmon-enhanced second-harmonic generation in graphene and semiconductor two-dimensional electron systems, Phys. Rev. B **84**, 045432 (2011).

[47] H. Rostami, M. I. Katsnelson, G. Vignale, and M. Polini, Gauge invariance and Ward identities in nonlinear response theory, Ann. Phys. (Amsterdam) **431**, 168523 (2021).

[48] I. Yudhistira, N. Chakraborty, G. Sharma, D. Y. H. Ho, E. Laksono, O. P. Sushkov, G. Vignale, and S. Adam, Gauge-phonon dominated resistivity in twisted bilayer graphene near magic angle, Phys. Rev. B **99**, 140302(R) (2019).

[49] T. Ando, Screening effect and impurity scattering in monolayer graphene, J. Phys. Soc. Jpn. **75**, 074716 (2006).

[50] K. Nomura and A. H. MacDonald, Quantum Hall Ferromagnetism in Graphene, Phys. Rev. Lett. **96**, 256602 (2006).

[51] S. Das Sarma, S. Adam, E. H. Hwang, and E. Rossi, Electronic transport in two-dimensional graphene, Rev. Mod. Phys. **83**, 407 (2011).

[52] K. J. Tielrooij, J. C. W. Song, S. A. Jensen, A. Centeno, A. Pesquera, A. Zurutuza Elorza, M. Bonn, L. S. Levitov, and F. H. L. Koppens, Photoexcitation cascade and multiple hot-carrier generation in graphene, Nat. Phys. **9**, 248 (2013).

[53] H. Rostami and E. Cappelluti, Impurity effects and bandgap closing in massive Dirac systems, Phys. Rev. B **96**, 054205 (2017).

[54] H. Rostami and E. Cappelluti, Dominant role of two-photon vertex in nonlinear response in two-dimensional Dirac systems, npj 2D Mater. Appl. **5**, 50 (2021).